

# Quantum solver for single-impurity Anderson models with particle-hole symmetry\*

M. Karabin<sup>1,2,†</sup> T. Sohail<sup>3</sup>, D. Bykov<sup>3</sup>, E. A. Coello Pérez<sup>3</sup>,‡ S. Ghosh<sup>3</sup>,

M. Gopalakrishnan Meena<sup>3</sup>, S. Kim<sup>3</sup>, A. Shehata<sup>3</sup>, I.-S. Suh<sup>3</sup>, H. Terletska<sup>1,2</sup>, and M. Eisenbach<sup>3</sup>

<sup>1</sup>*Department of Physics and Astronomy, Middle Tennessee State University, Murfreesboro, TN, USA*

<sup>2</sup>*Quantum Research Interdisciplinary Science and Education (QRISE) Center, Middle Tennessee State University, Murfreesboro, TN, USA and*

<sup>3</sup>*National Center for Computational Sciences, Oak Ridge National Laboratory, Oak Ridge, TN, USA*

(Dated: January 16, 2026)

Quantum embedding methods, such as dynamical mean-field theory (DMFT), provide a powerful framework for investigating strongly correlated materials. A central computational bottleneck in DMFT is in solving the Anderson impurity model (AIM), whose exact solution is classically intractable for large bath sizes. In this work, we develop and benchmark a quantum-classical hybrid solver tailored for DMFT applications, using the variational quantum eigensolver (VQE) to prepare the ground state of the AIM with shallow quantum circuits. The solver uses a unified ansatz framework to prepare the particle and hole excitations of the ground-state from parameter-shifted circuits, enabling the reconstruction of the impurity Green's function through a continued-fraction expansion. We evaluate the performance of this approach across a few bath sizes and interaction strengths under noisy, shot-limited conditions. We compare three optimization routines (COBYLA, Adam, and L-BFGS-B) in terms of convergence and fidelity, assess the benefits of estimating a quantum-computed moment (QCM) correction to the variational energies, and benchmark the approach by comparing the reconstructed density of states (DOS) against that obtained using a classical pipeline. Our results demonstrate the feasibility of Green's function reconstruction on near-term devices and establish practical benchmarks for quantum impurity solvers embedded within self-consistent DMFT loops.

## I. INTRODUCTION

Chemistry and condensed matter physics are governed by the collective behavior of interacting electrons [1]. Since the direct numerical solution of the Schrödinger equations is computationally intractable for all but the smallest systems, many different approaches have been devised that employ various approximations to reduce the computational complexity of solving the many-electron problem [2]. Among these, density functional theory (DFT) [3, 4] is a widely used and popular method that, while theoretically exact, relies on approximations to the exchange-correlation functional. These approximations often fail to capture strong local correlations, especially in systems exhibiting Mott physics or dynamical electron localization. One method to reintroduce electron correlation contributions missed by these approximations augments this approach with dynamical mean-field theory (DMFT) [5–9], which maps the lattice

model onto a local Anderson impurity model (AIM) [10–12], providing the mean-field that describes the electrons in a lattice. The impurity model captures local dynamical fluctuations and becomes exact in the limit of infinite spatial dimensions. This mapping has been highly instrumental in describing correlated electron materials ranging from transition metal oxides to heavy fermion systems.

Solving the AIM within DMFT typically requires computationally expensive techniques such as exact diagonalization, continuous-time quantum Monte Carlo, or numerical renormalization group. Although accurate, these classical solvers scale poorly with bath size and may struggle with real-frequency or sign problems [6, 13], limiting their application to more complex systems. Furthermore, these methods can also become computationally expensive at low temperatures [14, 15], where quantum entanglement and non-perturbative effects like the Kondo phenomenon play a crucial role.

Quantum computing introduces novel approaches to solving impurity models with the potential to overcome some of these limitations, owing to its ability to efficiently represent large Hilbert spaces and capture strong electron correlations [16, 17]. Some of these approaches construct a continued fraction representation of the model's Green's function [18, 19] from quantum states that represent the ground state of the AIM and the particle and hole excitations of such a state at the impurity sites. The limitation of circuit depth in current quantum hardware makes the optimization of shallow parametrized quantum circuits via the variational quantum eigensolver

\* **Notice:** This manuscript has been authored by UT-Battelle, LLC, under contract DE-AC05-00OR22725 with the US Department of Energy (DOE). The US government retains, and the publisher, by accepting the article for publication, acknowledges that the US government retains a nonexclusive, paid-up, irrevocable, worldwide license to publish or reproduce the published form of this manuscript, or allow others to do so, for US government purposes. DOE will provide public access to these results of federally sponsored research in accordance with the DOE Public Access Plan (<http://energy.gov/downloads/doe-public-access-plan>).

† [mariia.karabin@mtsu.edu](mailto:mariia.karabin@mtsu.edu)

‡ [coeloperea@ornl.gov](mailto:coeloperea@ornl.gov)

(VQE) [20, 21] a common strategy to prepare the AIM ground state in the noisy intermediate-scale quantum era.

In this work, we evaluate the performance of a quantum solver for AIMs that incorporates multiple quantum subroutines to reconstruct the impurity Green's function. We first introduce a minimal yet expressive variational ansatz capable of preparing the model's ground state, as well as the particle and hole excitations needed to compute the impurity Green's function. We benchmark variational results against exact diagonalization to assess the accuracy and robustness of this ground-state preparation method. The corresponding excited states are generated via structured parameter shifts applied to the optimized ground-state circuit, avoiding the need to re-optimize each excited state. The performance of the proposed solver is evaluated by computing the impurity Green's functions for multiple values of the Hubbard interaction and bath sizes. Finally, we analyze the computational overhead associated with different variational optimization strategies, including COBYLA, Adam, and L-BFGS-B in the presence of finite sampling noise. These resource estimates provide realistic expectations for embedding this quantum solver into DMFT workflows.

The remainder of this paper is organized as follows. In Section II, we describe the methods used to calculate the continued fraction representation of the impurity Green's function, present the ansatz architecture employed to approximate the ground and excited states of the AIM, and introduce the tested optimization routines. Section III reports our numerical results, including variational ground-state preparation, the fidelity and cost of optimization, moment-based energy corrections, and Green's function reconstruction. We conclude in Section IV with a summary of our findings and a discussion of future directions for integrating quantum impurity solvers within dynamical mean-field theory workflows.

## II. METHODS

In this section, we outline the workflow developed to compute the impurity Green's function. We first define the Hamiltonian used to model the interacting impurity coupled to a non-interacting bath, followed by a description of the ansatz used to approximate its ground state via VQE and the methods used to optimize it. To improve the variational energy estimates, we discuss how to incorporate leading corrections derived from a cumulant expansion based on low-order Hamiltonian moments. Finally, we extend the ansatz to approximate particle and hole excitations by extending the optimized ground-state circuit, and describe the Krylov subspace procedure used to approximate the continued-fraction representation of the impurity Green's function.

### A. The impurity model

This work focuses on single-impurity Anderson models defined by the Hamiltonian [10]

$$\begin{aligned} H_{\text{AIM}} &= H_{\text{imp}} + H_{\text{bath}} + H_{\text{coup}}, \\ H_{\text{imp}} &= \sum_{\sigma} \epsilon_0 n_{0\sigma} + U n_{0\uparrow} n_{0\downarrow}, \\ H_{\text{bath}} &= \sum_{k=1}^{N_b} \sum_{\sigma} \epsilon_k n_{k\sigma}, \\ H_{\text{coup}} &= \sum_{k=1}^{N_b} \sum_{\sigma} V_k (c_{0\sigma}^{\dagger} c_{k\sigma} + c_{0\sigma} c_{k\sigma}^{\dagger}), \end{aligned} \quad (1)$$

where  $\epsilon_0$  and  $\epsilon_k$  are the single-particle energies of the impurity and the  $k$ -th bath site, respectively,  $U$  the Hubbard interaction,  $V_k$  is the hybridization between the impurity and the  $k$ -th bath sites,  $N_b \in \{1, 3, 5\}$  is the number of bath sites, and  $\sigma \in \{\uparrow, \downarrow\}$  is the projection of the electron's spin. The operators  $c_{i\sigma}^{\dagger}$  and  $c_{i\sigma}$  create and annihilate an electron with spin projection  $\sigma$  in site  $i$ . The number operators  $n_{i\sigma}$  count the number of  $\sigma$ -electrons in orbital  $i$ .

In this work, we impose particle-hole symmetry on the Hamiltonian by setting  $\epsilon_0 = -U/2$ , ensuring the system is half-filled, and its ground state has spin projection  $S_z = 0$  in the absence of an external magnetic field, and set  $V_k = V$  for all  $k$ .

These impurity models form the foundation of DMFT, which maps the original interacting lattice problem onto a self-consistently defined quantum impurity coupled to a non-interacting bath. This mapping retains all local interaction effects while approximating non-local correlations. The interaction between the impurity and the bath is described by the hybridization function, which reflects the dynamical coupling to the environment and must be updated iteratively through the DMFT loop. In practical implementations, this continuous bath is discretized into a finite number of orbitals, making the bath size a crucial control parameter. As the bath size increases, the model captures finer dynamical features, but also becomes increasingly challenging to solve. These challenges motivate the development of quantum impurity solvers [22, 23] capable of efficiently handling large Hilbert spaces and providing direct access to real-frequency observables.

Solving the impurity problem in DMFT involves computing the impurity Green's function [5, 6], which as a function of the energy  $\omega$  takes the form

$$\begin{aligned} G_{ij}(\omega) &= \langle \psi_0 | c_i \frac{1}{\omega - H_{\text{AIM}} + E_0} c_j^{\dagger} | \psi_0 \rangle \\ &+ \langle \psi_0 | c_j^{\dagger} \frac{1}{\omega + H_{\text{AIM}} - E_0} c_i | \psi_0 \rangle. \end{aligned} \quad (2)$$

Here, the ground state  $\psi_0$  of the AIM Hamiltonian (1) solves the Schrödinger equation

$$H_{\text{AIM}} |\psi_0\rangle = E_0 |\psi_0\rangle. \quad (3)$$

Therefore, computing the impurity Green's function involves finding the ground state of the AIM (1), calculating its energy, and evaluating the matrix elements on the right-hand side of Eq. (2).

### B. Variational ground state approximation

Our quantum solver employs VQE to optimize a parameterized quantum circuit (PQC), minimizing the variational energy

$$E_{\text{VQE}}(\boldsymbol{\theta}) = \min_{\boldsymbol{\theta}} \langle \psi(\boldsymbol{\theta}) | H_{\text{AIM}} | \psi(\boldsymbol{\theta}) \rangle, \quad (4)$$

to find an approximation  $|\boldsymbol{\theta}\rangle$  to the model's ground state  $|\psi_0\rangle$ . To this end, the Hamiltonian (1) is recast in terms of spin operators using the Jordan–Wigner transformation [24, 25],

$$\begin{aligned} c_i^\dagger &= \prod_{j=0}^{i-1} Z_j \otimes \frac{1}{2}(X_i - iY_i) \otimes \cdots \\ c_i &= \prod_{j=0}^{i-1} Z_j \otimes \frac{1}{2}(X_i + iY_i) \otimes \cdots, \end{aligned} \quad (5)$$

where  $X_i$ ,  $Y_i$  and  $Z_i$  are Pauli matrices acting on the space of qubit  $i$ , which encodes the occupation of a single spin-orbital in the model.

Using the orbital-to-qubit mapping depicted in Fig. 1 to assign qubits along a linear chain to the model's spin-

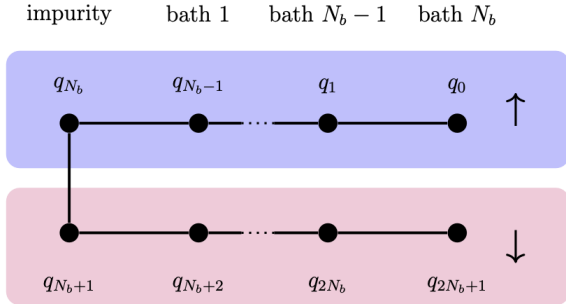


FIG. 1. Spin-block ordering used to map the model's spin-up and down sites onto a linear chain of qubits.

orbitals leads to the expression

$$\begin{aligned} H_{\text{AIM}} = & C - \sum_{k=1}^{N_b} \frac{\epsilon_k}{2} (Z_{N_b-k} + Z_{N_b+1+k}) + \frac{U}{4} Z_{N_b} Z_{N_b+1} \\ & + \frac{V}{2} \sum_{k=1}^{N_b} X_{N_b-k} \left( \prod_{j=N_b+1-k}^{N_b-1} Z_j \right) X_{N_b} \\ & + \frac{V}{2} \sum_{k=1}^{N_b} Y_{N_b-k} \left( \prod_{j=N_b+1-k}^{N_b-1} Z_j \right) Y_{N_b} \\ & + \frac{V}{2} \sum_{k=1}^{N_b} X_{N_b+1} \left( \prod_{j=N_b+2}^{N_b+k} Z_j \right) X_{N_b+1+k} \\ & + \frac{V}{2} \sum_{k=1}^{N_b} Y_{N_b+1} \left( \prod_{j=N_b+2}^{N_b+k} Z_j \right) Y_{N_b+1+k}, \end{aligned} \quad (6)$$

where  $C = -U/4 + \sum_{k=1}^{N_b} \epsilon_k$ . The expectation value (4) is calculated adding the expectation values of each term in the Pauli-strings decomposition of the Hamiltonian, which can be estimated on a quantum chip by measuring the state  $\psi(\boldsymbol{\theta})$  in the  $N_{\text{group}}$  bases corresponding to the commuting groups into which the Pauli strings are organized. The absolute error associated with the finite sampling of the state is estimated as

$$\varepsilon \sim \mathcal{O} \left( \sqrt{N_{\text{Pauli}}/N_{\text{shots}}} \right), \quad (7)$$

where  $N_{\text{Pauli}}$  and  $N_{\text{shots}}$  denote the number of Pauli strings defining the Hamiltonian and the number of measurements taken on each basis [26, 27].

The symmetries of the ground state arising from that imposed on the Hamiltonian allow us to propose a highly constrained PQC as an ansatz for the ground state. Following Ref. [28], we construct this ansatz from half-filling gates, which initialize a state with the appropriate number of spin-up and spin-down electrons, and Givens rotations that enlarge the subspace accessible to the ansatz. The quantum circuits on the top left and top right of Fig. 2 implement the half-filling and Givens rotation gates, respectively. While the first of these gates “creates” an electron in a spin-orbital pair, the second one implements a two-qubit rotation that does not change electron number. Our ansatz for the ground states of the single-impurity AIMs with one and three bath sites are respectively shown on the bottom left and bottom right of Fig. 2. Notice that the ansatz for the one-bath case is embedded within that for the three-bath case.

### C. Optimization methods

The estimation of the variational energy depends on finding the parameters that best approximate the ground state, making the choice of optimizer critical for the efficient and accurate computation of this observable.

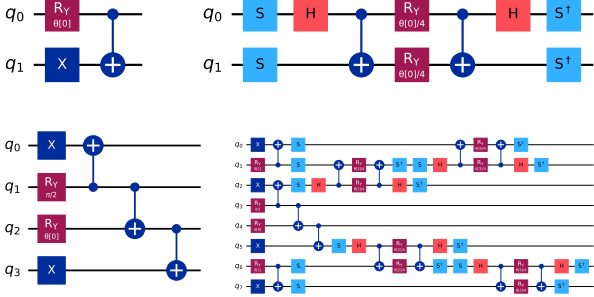


FIG. 2. Half-filling (top left) and Givens rotation (top right) gates used to construct ansatz for the ground states of single-impurity AIMs. Ansatz for the ground states of single-impurity AIMs with one (bottom left) and three (bottom right) bath sites.

Different optimization strategies navigate the parameter landscape in distinct ways, each presenting trade-offs between convergence speed, sensitivity to sampling noise, and computational cost. To identify the most effective approach, we examined three representative optimization strategies employing gradient-free, first-order, and quasi-second-order methods.

The constrained optimization by linear approximation (COBYLA) gradient-free method [29] constructs a local linear model of the objective function by evaluating it at a dynamical number of parameter points located within a hypersphere of radius  $\rho_0$ , set in this work to  $\pi$ , centered at the initial point. The parameters that minimize this model are then chosen as a new center, and the procedure is repeated for a new radius,  $\rho_1 < \rho_0$ . Hence, gradient-free optimizers has the lowest measurement cost per evaluation, requiring only the  $N_{\text{group}}$  circuit measurements needed to estimate the energy.

Adam was selected as a representative first-order optimizer [30]. Gradient-based methods update the parameters along the direction of the negative gradient, estimated on a quantum computer using the parameter-shift rule,

$$\frac{\partial E_{\text{VQE}}}{\partial \theta_i} \Big|_{\theta} = \frac{1}{2} [E_{\text{VQE}}(\theta_i^+) - E_{\text{VQE}}(\theta_i^-)], \quad (8)$$

with  $\theta_i^\pm$  a set of parameters in which the  $i$ -th component of  $\theta$  is set to  $\theta_i \pm \pi/2$ . Although the number of measurements per evaluation,  $N_{\text{group}}(1 + 2N_{\text{params}})$ , is substantially higher than that for gradient-free methods, first-derivative information may help these optimizers converge the VQE in fewer overall evaluations. Our Adam optimizations used an initial learning rate  $\eta = 1$ , standard hyperparameters  $\{\beta_1, \beta_2, \epsilon\} = \{0.9, 0.999, 10^{-8}\}$ , and initialized all momentum terms to zero.

For comparison, we also tested the quasi-second-order limited-memory Broyden-Fletcher-Goldfarb-Shanno (L-BFGS-B) algorithm [31], which approximates the inverse Hessian from a limited number of past gradient estimates.

In this context, the number of measurements per evaluation is that of a first-order gradient-based method.

Convergence for all optimizers was defined as either an absolute estimate change  $|E_{\text{VQE}}^{(n)} - E_{\text{VQE}}^{(n-1)}| < 10^{-6}$ , with  $E_{\text{VQE}}^{(n)}$  the energy estimated at iteration  $n$ , or a gradient norm  $\|\nabla_{\theta} E_{\text{VQE}}^{(n)}\| < 10^{-9}$ .

#### D. Quantum computed moments (QCM) approach

A key limitation of the VQE is that the extent to which the state  $\psi(\theta)$  and the estimated energy  $E_{\text{VQE}}$  approximate the true ground state and its energy strongly depends on the expressive power of the chosen ansatz and the convergence of the optimization routine. The latter is severely affected by errors in the expectation value and the presence of barren plateaus.

The QCM approach proposed in Ref. [32] addresses this limitation by estimating a correction to the variational energy from higher-order Hamiltonian moments  $\langle H^m \rangle = \langle \psi(\theta) | H^m | \psi(\theta) \rangle$ . In terms of a set of cumulants  $c_m$ , defined as

$$c_m = \langle H^m \rangle - \sum_{p=0}^{m-2} \binom{m-1}{p} c_{p+1} \langle H^{m-1-p} \rangle, \quad (9)$$

the Lanczos coefficients [33] defining the tridiagonal Hamiltonian in the Krylov basis built on  $\psi(\theta)$ ,

$$H_{\text{AIM}} = \begin{pmatrix} a_0 & b_1 & 0 & \dots \\ b_1 & a_1 & b_2 & \dots \\ 0 & b_2 & a_3 & \dots \\ \vdots & \vdots & \vdots & \ddots \end{pmatrix}, \quad (10)$$

can be written as expansions in powers of  $1/N$  [34],

$$\begin{aligned} a_\ell &= c_1 + \ell \left( \frac{c_3}{c_2} \right) \frac{1}{N} + \mathcal{O}(N^{-2}) \\ b_\ell^2 &= \ell c_2 + \frac{1}{2} \ell(\ell-1) \left( \frac{c_2 c_4 - c_3^2}{2c_2^2} \right) \frac{1}{N} + \mathcal{O}(N^{-2}), \end{aligned} \quad (11)$$

with  $N$  the size of the system. For large  $\ell$  and  $N$ , these expansions become series in powers of  $z = \ell/N$ , in terms of which the ground-state energy can be calculated as the infimum of  $a(z) - 2b(z)$  for  $z > 0$  [35, 36]. At first order in  $z$ , this infimum takes the approximate form

$$E_{\text{INF}} \approx c_1 - \frac{c_2^2}{c_3^2 - c_2 c_4} \left( \sqrt{3c_3^2 - 2c_2 c_4} - c_3 \right). \quad (12)$$

Notice that this approximation, although no longer a strict upper bound, incorporates corrections from higher-order Hamiltonian moments in its second term, yielding a more accurate estimate of the true ground-state energy than the variational result alone. From a computational perspective, this approach shifts part of the problem complexity away from deep, highly expressible circuits to the measurement of higher-order observables.

Corrections to the ground-state energy are particularly relevant within the context of DMFT, as the accurate determination of this quantity is important to stabilize the self-consistency loop. By incorporating higher Hamiltonian moments, one can potentially mitigate errors due to shallow ansatz, sampling noise, and barren plateaus.

### E. Green's function as continued fractions

In order to extract physically meaningful observables from the quantum-computed ground and excited states of the AIM, we reconstruct the impurity Green's function in the real-frequency domain using a Krylov subspace-based continued-fraction expansion.

Since the model lacks coupling between spin-up and spin-down orbitals, the off-diagonal elements of the impurity Green's function (2) vanish identically. The diagonal matrix elements can be expressed as continued fractions [37]

$$G_{ii}(\omega) = \frac{1}{\omega + E_0 - a_0^p - \frac{(b_1^p)^2}{\omega + E_0 - a_1^p - \dots}} + \frac{1}{\omega - E_0 + a_0^h - \frac{(b_1^h)^2}{\omega - E_0 + a_1^h - \dots}}, \quad (13)$$

where  $a_n^p$  and  $b_n^p$  are the Lanczos coefficients of  $H_{\text{AIM}}$  on the Krylov basis built on top of  $c_i^\dagger |\psi_0\rangle$ , and  $a_n^h$  and  $b_n^h$  the corresponding coefficients on the basis built on top of  $c_i |\psi_0\rangle$ .

The ansatz on the left and right sides of Fig. 3 prepare states with one particle and three particles, respectively. It can be shown that setting their parameters to  $\pi - \theta_0$ ,

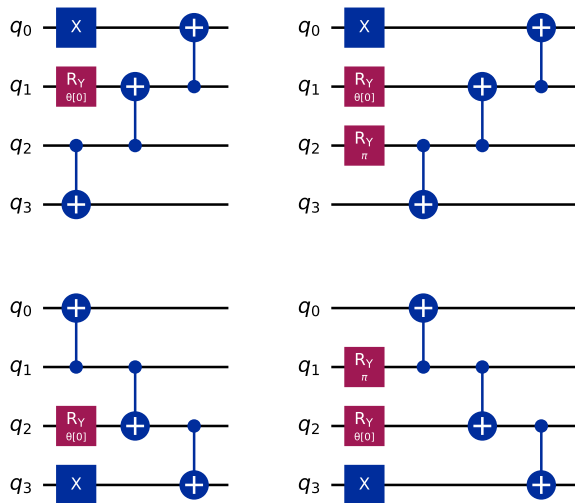


FIG. 3. Ansatz for the particle (right) and hole (left) excitations of single-bath AIM ground-states preparing states with spin projection  $S_z = \frac{1}{2}$  (top) and  $S_z = -\frac{1}{2}$  (bottom).

generates the particle and hole excitations corresponding to the one-bath ground state prepared by  $\theta_0$ . Moreover, substituting the one-bath ground-state ansatz within the three-bath ansatz with those designed to prepare one-bath excitations yields the corresponding three-bath excitations. This result holds for the five-bath case as well.

Using the ansatz for the particle and hole excitations, we can approximate the Lanczos coefficients in Eq. (13) by truncating their cumulant expansions (11) to order  $1/N$ , using estimates for the expectation values of powers of the Hamiltonian up to  $n = 4$ .

### F. Classical Reference Calculations

To validate our quantum ansatz, we also perform classical calculations of the Green's function. For the model sizes investigated in the present paper, exact diagonalization of the Hamiltonian is easily accomplished without the need for high-performance computing resources. We follow the procedure outlined in section II E above to represent the Green's function as a continued fraction with its coefficients being determined using Lanczos iteration. For this, we first construct a basis for the ground state calculations, which consists of all sets of creation operators that preserve the total charge and spin for the half-filled system considered here, i.e. a total of  $2 \binom{N_b+1}{(N_b+1)/2}$  of basis states. The Hamiltonian for the AIM can be represented as a sparse matrix and we first find the lowest eigenvalue state  $|\psi_0\rangle$  with the ground state energy  $E_0$ . Using this, we can apply creation or annihilation operators to this vector and follow equation 2 to calculate the many-body Green's function using the continued fraction in equation 13, where the coefficients can be obtained using Lanczos iteration. [37, 38]

## III. RESULTS

The results presented in this section, used to assess the performance of the proposed quantum solver, were obtained from classical simulations of the quantum subroutines involved in the computation of the impurity Green's function (2). These simulations solved the AIM described in Section II A, with Hubbard interactions  $U \in \{2, 4, 6, 8\}$ . To account for the potential for the optimizer to become trapped in local minima, the VQE results for the 1- and 3-bath cases reported here are averaged over simulations initiated from ten distinct starting points. Moreover, each optimization was repeated five times to mitigate statistical errors arising from the finite number of shots used to evaluate the variational estimates. For the more computationally demanding 5-bath case, simulations were performed using a single initialization, with two optimization repeats. The scalability of the solver with respect to the number of bath sites is assessed by averaging results over the different values of  $U$ . As discussed in Section II C, the ansatz was optimized

using a gradient-free method (COBYLA), a first-order gradient-based method (Adam), and a quasi-second-order gradient-based method (L-BFGS-B) to compare the performance of different optimization strategies.

### A. Ground-state optimization

The ansatz proposed for the ground state does not span the full  $n$ -qubit Hilbert space and therefore may struggle to approximate the ground state of the AIM as the number of bath sites increases. To assess the performance of this ansatz, we compared ground-state energies obtained via classical diagonalization with those produced by ideal VQE simulations. Figure 4 shows the absolute relative errors  $\delta E \equiv \text{abs}([E_{\text{ideal}} - E_{\text{exact}}]/E_{\text{exact}})$  produced by these simulations. For AIMs with five bath sites, the

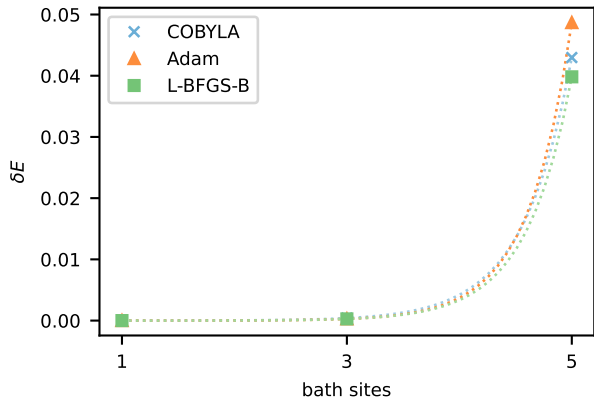


FIG. 4. Absolute relative error between the exact ground-state energy and its variational estimate. For impurity models with five bath sites, the proposed ansatz yields energy estimates accurate to within about five percent of the exact ground-state energy.

ansatz was capable of yielding variational energies that deviate from the exact ground-state energy by approximately five percent.

In practice, the variational energy is estimated from a finite number of measurements, causing sampling noise that may impede convergence to the best achievable approximation of the ground state. To quantify this effect, we performed VQE simulations with a varying number of shots for AIMs with one and three bath sites and Hubbard interaction  $U = 2$ . The resulting absolute relative errors,  $\delta E \equiv \text{abs}([E_{\text{samp}} - E_{\text{ideal}}]/E_{\text{ideal}})$ , are shown in Fig. 5.

These values show that for all three optimizers, the energy error decreases as the number of shots per commuting group increases. The rate and stability of this improvement depend strongly on whether gradients are used in the optimization. Across the range of shots, COBYLA exhibits large errors, indicating that noise in the energy estimates can easily trap the gradient-free

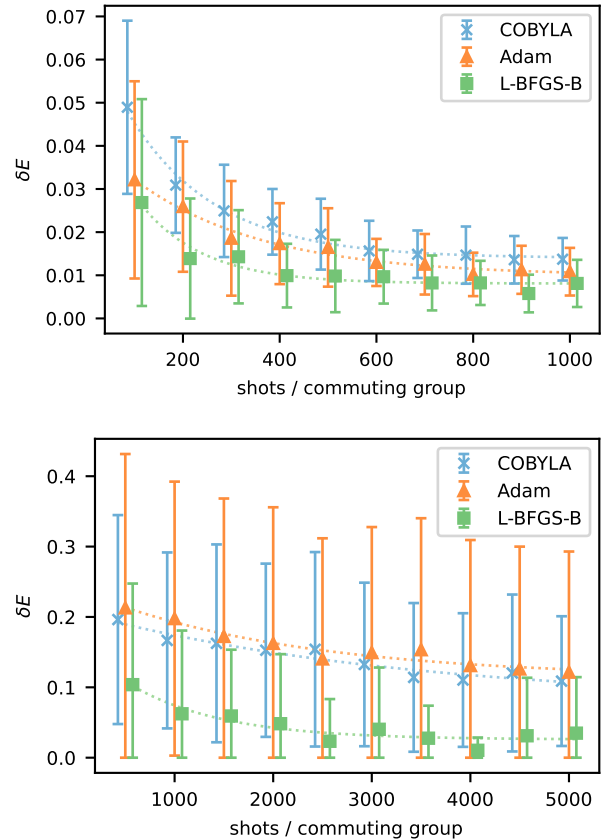


FIG. 5. Absolute relative error between variational energies from simulations with and without sampling noise. These simulations solved AIMs with one (top) and three (bottom) bath sites and on-site energy  $U = 2$ . The shown mean values and standard deviations result from simulations initiated from ten distinct starting points, each repeated five times to account for sampling errors.

search in local minima. In contrast, our results suggest that gradient-based methods can achieve higher accuracy, but doing so requires information about second derivatives. For the best performing optimization method (L-BFGS-B), relative differences of roughly two percent are achieved in the one- and three-bath cases from 100 and 2500 measurements per quantum circuit, respectively. This behavior highlights that reliable gradient information and accurate Hessian approximations are crucial to avoid noise-induced convergence to suboptimal states.

Using relation (7), we estimate that absolute energy errors of  $\epsilon \sim 0.1$  can be achieved with 700, 2500, and 5000 shots per commuting group for AIMs with one, three, and five bath sites, respectively.

## B. Optimization performance, fidelity, and cost

We use the number of circuit executions required to converge the VQE as a metric of the subroutine's quantum cost. Figure 6 shows the scaling of this cost with the number of bath sites for three different optimization methods. The costs presented there, which are averages

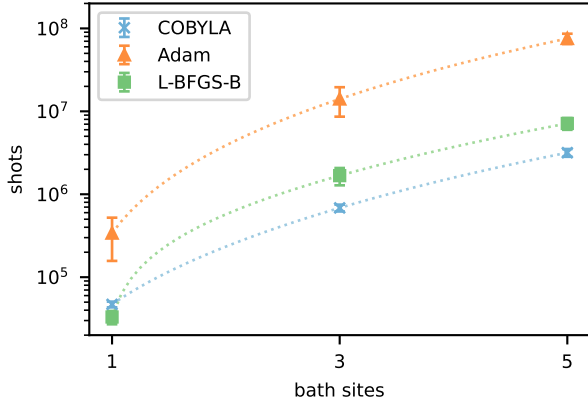


FIG. 6. Comparison between total number of shots required by different optimization methods to converge VQEs solving single-impurity AIMs with  $N_b \in \{1, 3, 5\}$ .

over all runs that solved AIMs with the corresponding number of bath sites, highlight the differences in computational expense between the tested optimization methods.

The COBYLA optimizer measures the lowest number of circuits per evaluation and thus exhibits the best scaling with  $N_b$ . Unfortunately, without the computation of a gradient pushing in the direction of maximum change, the objective function tends to get stuck in local minima, as reflected by the larger  $\delta E$  values for this method in Fig. 5. The gradient-based Adam and L-BFGS-B optimizers substantially increase the number of circuit measurements per evaluation, leading to worse scaling than that of COBYLA. Furthermore, results in Fig. 5 from runs using the Adam optimizer suggest that sampling errors in the gradient estimate can push the optimization towards local minima, yielding larger  $\delta E$  values. This effect seems to be mitigated via the estimation of the inverse Hessian carried on by the L-BFGS-B optimizer.

These cost differences are considered together with the accuracy results discussed in Sec. III A. In ideal simulations, the proposed ansatz produces ground-state energies that differ from the exact values by at most a few percent for  $N_b \leq 5$ , as shown in Fig. 4, indicating that the ansatz retains a reasonable ground-state fidelity across the range of bath sizes we studied. In the presence of sampling noise, COBYLA is more prone to being trapped in shallow local minima, especially at low shot counts. This leads to larger energy errors despite its lower circuit cost. The gradient-based optimizers make more efficient use of the measurement statistics. For a

fixed target accuracy, they achieve smaller relative energy errors at moderate shot numbers, with L-BFGS-B providing the most favorable balance between accuracy and quantum cost.

These results highlight a trade-off between circuit depth, optimizer robustness, and measurement overhead. Gradient-free methods minimize the raw number of circuits but can incur a significant accuracy penalty, particularly when measurements are noisy. Gradient-based methods require more circuits but deliver higher-fidelity approximations to the impurity ground state.

## C. Energy correction estimates

As discussed in Sec. II B, the variational energy can be refined by incorporating higher-order Hamiltonian moments measured in the optimal state. Starting from the moments  $\langle H^n \rangle$  up to  $n = 4$ , we used the approximation to the infimum (12). This approximation corrects the raw variational estimate  $c_1$  with fluctuations encoded in  $c_2$ ,  $c_3$ , and  $c_4$ , which capture increasingly nontrivial dynamical correlations beyond those described by the shallow ansatz alone.

For consistency, the number of shots used to estimate  $\langle H^4 \rangle$  is increased to achieve an absolute error of  $\epsilon \sim 10^{-1}$ . These numbers are listed in Table I. From those, the total number of shots required to compute the correction to the variational energy are  $1.4 \times 10^3$ ,  $1.53 \times 10^6$ , and  $7.6 \times 10^7$  for the one, three, and five-bath cases.

$N_b$	$N_{\text{Pauli}}$				$N_{\text{group}}$	$N_{\text{shots}}$	
	$H$	$H^2$	$H^3$	$H^4$		$H$	$H^4$
1	6	12	22	23	2	700	700
3	18	122	502	1192	51	2.5K	30K
5	30	360	2542	10997	304	5K	250K

TABLE I. Number of Pauli strings in  $\langle H^n \rangle$  up to  $n = 4$ , number of commuting groups in  $\langle H^4 \rangle$ , and number of shots per group required to achieve absolute errors  $\epsilon \sim 10^{-1}$  on the estimates for  $\langle H \rangle$  and  $\langle H^4 \rangle$ .

The AIMs considered here provide a controlled setting to assess the effectiveness of this correction, since the exact ground-state energies are available from classical diagonalization. For each VQE run, we compute the absolute relative error, both for the bare variational estimate  $E_{\text{VQE}}$  and the infimum approximation  $E_{\text{INF}}$ . As shown in Fig. 7, the correction estimate systematically reduces the absolute relative error introduced by both ansatz limitations and sampling noise. For the gradient-free optimal states, the correction yields a substantial reduction for both the three- and five-bath cases, indicating that higher-order moments can partially recover correlation energy that the variational state fails to capture. Gradient-based optimizations already yield smaller variational errors, particularly L-BFGS-B, yet, they also benefit from the correction. The largest relative gains appear

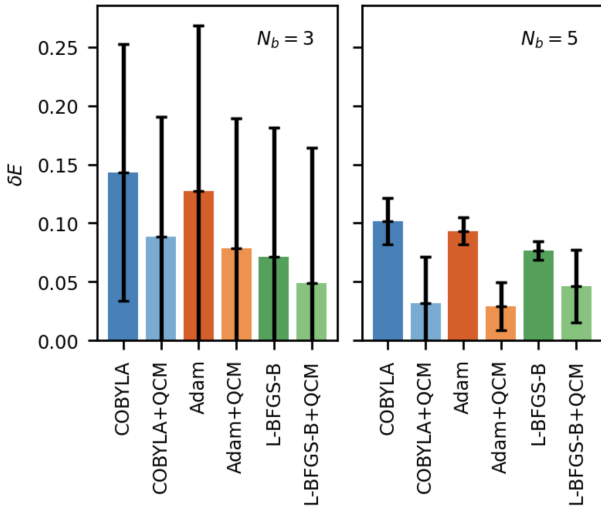


FIG. 7. Average absolute relative error  $\delta E$  between the exact ground-state energy and its numerical estimate for AIMs with three (left) and five (right) bath sites. Bars compare the variational energies obtained with COBYLA, Adam, and L-BFGS-B to the corresponding QCM-corrected estimates (“+QCM” labels). Each bar is averaged over all interaction strengths and random initializations.

in the larger-bath regimes. Computation of the QCM correction requires additional measurements to estimate higher-order Hamiltonian moments. For the three-bath case, this overhead is comparable to the VQE optimization cost for the L-BFGS-B optimizer, as shown in Fig. 6. In the five-bath case computing this correction is more expensive than solving the variational problem.

Since the QCM energy is not constrained to the upper bound, it can overshoot the energy for individual runs. However, the cumulant-based estimate provides, on average, a closer approximation to the exact ground-state energy. In the DMFT context, this improvement in the impurity ground-state energy is particularly valuable, as it can improve the stability of the self-consistency loop without requiring deeper ansatz for the ground state.

#### D. Green’s function reconstruction

To assess the accuracy with which the proposed solver can reconstruct the impurity Green’s function, we estimated the approximate particle and hole Lanczos coefficients (11) from Hamiltonian moments computed on the states prepared by the ansatz for the particle and hole excitations. These estimates were computed for every parameter set found by simulated VQE runs optimized via the L-BFGS-B algorithm, and averaged to obtain mean values for the Lanczos coefficients for a given number of bath sites and Hubbard interaction.

The resulting Lanczos coefficients were used to construct an averaged continued-fraction representation of the Green’s function for each AIM. From this represen-

tation, we then computed the corresponding density of states (DOS),

$$\text{DOS}(\omega) = -\frac{1}{\pi} \text{Im}\{\text{Tr}[G(\omega)]\}, \quad (14)$$

and compared it with the DOS obtained from the exact Lanczos coefficients computed classically from the particle and hole excitations of the ground state determined via classical diagonalization.

This comparison is shown in Fig. 8. The peaks in the DOS for one-bath AIMs, shown at the top of the figure, are reproduced with very good accuracy for weak Hubbard interactions, as shown in the top row of the figure. As the interaction strength increases, the spectrum progressively splits into lower- and upper-Hubbard-like features, and the sampled DOS tracks the relative weight of these peaks across all interaction values. The sampled DOS for three-bath AIMs, shown in the middle row of Fig. 8, captures the main features of the exact DOS over the full frequency window. This shows that, once a reasonably accurate variational ground state has been obtained, the combination of excited-state ansatz and Lanczos-based continued fractions yields a reasonable and compact representation of the impurity Green’s function. We extended our simulations to also a 5-bath AIM. Due to the significantly higher cost and deeper quantum circuits, the 5-bath case was evaluated using a reduced number of configurations. Specifically, only one initialization seed was used, and the optimization was repeated twice to gather statistical information. These results provide valuable insight into the applicability of our ansatz and VQE-based reconstruction to larger systems. The reconstructed Green’s function, shown in Fig. 8, retains qualitative spectral features, although with increased variance due to sampling noise and circuit optimization. The ability to carry out this reconstruction without further ansatz tuning shows the generalizability of our excitation-preparation approach across increasing bath sizes.

The additional measurements needed to estimate the Lanczos coefficients and evaluate the continued fractions result in a quantum cost comparable to that of the VQE optimization in the three-bath case. For larger AIMs, however, this subroutine becomes the dominant cost, as the number of Pauli strings appearing in  $H^4$  grows rapidly with the number of bath sites.

## IV. OUTLOOK

This work presents a hybrid quantum-classical solver for computing the impurity Green’s function using quantum-prepared ground and excited states of the Anderson impurity model. By leveraging an ansatz framework that reuses ground-state parameters to generate particle and hole excitations, we demonstrate that continued-fraction Green’s function representations can be efficiently built using shallow quantum circuits. The

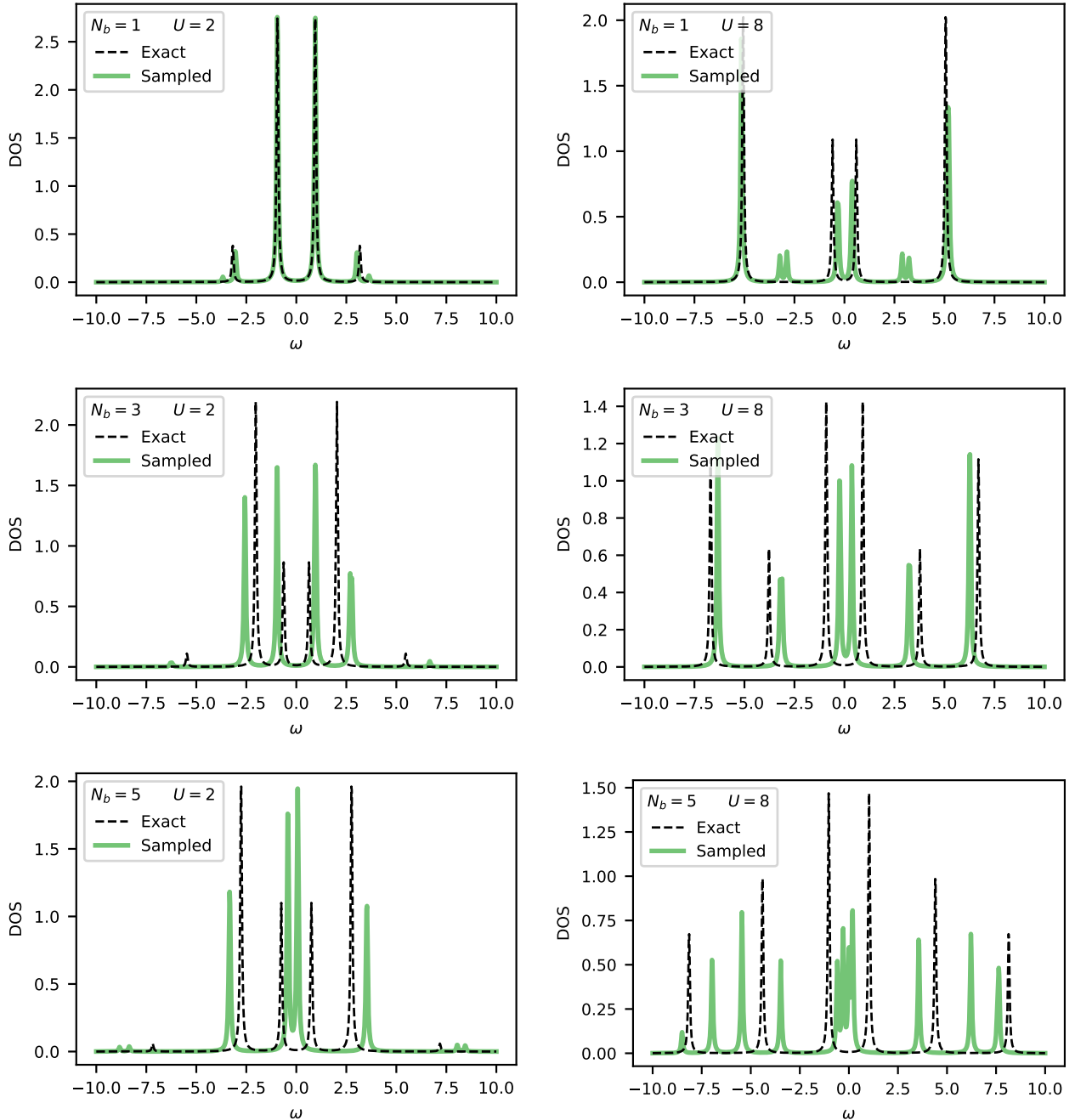


FIG. 8. Comparison between the DOS constructed using the proposed quantum solver (green solid lines) and a classical pipeline (black dashed lines). The shown density of states corresponds to AIMs with one (top), three (middle) and five (bottom) bath sites, with Hubbard interactions  $U = 2$  (left) and  $U = 5$  (right).

fidelity of the generated particle and hole excitations remains sufficiently high to construct Krylov subspaces, even when reusing ground-state parameters. The impurity Green's function reconstructed from these states exhibits good agreement with exact results, and their moments yield reliable quantum cumulant corrections. By evaluating and comparing the performance of multiple classical optimization techniques, we provide practi-

cal insights into the cost-performance trade-offs that will govern VQE-based quantum solvers.

A key extension of this work will involve incorporating the quantum impurity solver into a fully self-consistent DMFT loop as well as a first-principles DFT+DMFT workflow. Such integrations would allow us to tackle correlated real materials while maintaining a quantum-accurate treatment of local electron interactions. Fur-

thermore, addressing challenges of scalability and error resilience will require the incorporation of error mitigation techniques to offer more robust performance on noisy intermediate-scale quantum devices.

In summary, the approach developed here expands the emerging toolbox of hybrid quantum-classical many-body solvers and provides a viable pathway toward the accurate computation of real-frequency observables in strongly correlated systems, complementing existing classical methods.

## ACKNOWLEDGMENTS

The authors thank D. Rogers and P. Groszkowski for useful discussions. This research has been supported

by the National Science Foundation grants DMREF 2323546, DMREF 2323548, and used resources of the Oak Ridge Leadership Computing Facility at the Oak Ridge National Laboratory, which is supported by the Office of Science of the U.S. Department of Energy under Contract No. DE-AC05-00OR22725. HT is supported by the National Science Foundation under Grant No. QIS-2328752. MK is supported by the National Science Foundation under Grant No. 2538963.

---

[1] P. Fulde, *Electron Correlations in Molecules and Solids*. Springer Nature, 1995. [Online]. Available: <https://link.springer.com/book/10.1007/978-3-642-57809-0>

[2] M. Rossmannek, F. Pavović, A. Rubio, and I. Tavernelli, “Quantum embedding method for the simulation of strongly correlated systems on quantum computers,” *The Journal of Physical Chemistry Letters*, vol. 14, no. 14, pp. 3491–3497, 2023. [Online]. Available: <https://doi.org/10.1021/acs.jpclett.3c00330>

[3] P. Hohenberg and W. Kohn, “Inhomogeneous electron gas,” *Phys. Rev.*, vol. 136, pp. B864–B871, Nov 1964. [Online]. Available: <https://link.aps.org/doi/10.1103/PhysRev.136.B864>

[4] W. Kohn and L. J. Sham, “Self-consistent equations including exchange and correlation effects,” *Phys. Rev.*, vol. 140, pp. A1133–A1138, Nov 1965. [Online]. Available: <https://link.aps.org/doi/10.1103/PhysRev.140.A1133>

[5] G. Kotliar, S. Y. Savrasov, K. Haule, V. S. Oudovenko, O. Parcollet, and C. A. Marianetti, “Electronic structure calculations with dynamical mean-field theory,” *Rev. Mod. Phys.*, vol. 78, pp. 865–951, Aug 2006. [Online]. Available: <https://link.aps.org/doi/10.1103/RevModPhys.78.865>

[6] A. Georges, G. Kotliar, W. Krauth, and M. J. Rozenberg, “Dynamical mean-field theory of strongly correlated fermion systems and the limit of infinite dimensions,” *Rev. Mod. Phys.*, vol. 68, pp. 13–125, Jan 1996. [Online]. Available: <https://link.aps.org/doi/10.1103/RevModPhys.68.13>

[7] D. Zgid and G. K.-L. Chan, “Dynamical mean-field theory from a quantum chemical perspective,” *The Journal of Chemical Physics*, vol. 134, no. 9, p. 094115, 03 2011. [Online]. Available: <https://doi.org/10.1063/1.3556707>

[8] B. Bauer, D. Wecker, A. J. Millis, M. B. Hastings, and M. Troyer, “Hybrid quantum-classical approach to correlated materials,” *Phys. Rev. X*, vol. 6, p. 031045, Sep 2016. [Online]. Available: <https://link.aps.org/doi/10.1103/PhysRevX.6.031045>

[9] I. Rungger, N. Fitzpatrick, H. Chen, C. Alderete, H. Apel, A. Cowtan, A. Patterson, D. Muñoz Ramo, Y. Zhu, N. Nguyen, E. Grant, S. Chretien, L. Wossnig, N. Linke, and R. Duncan, “Dynamical mean field theory algorithm and experiment on quantum computers,” *Quantum*, Jan. 2020.

[10] P. W. Anderson, “Localized magnetic states in metals,” *Phys. Rev.*, vol. 124, pp. 41–53, Oct 1961. [Online]. Available: <https://link.aps.org/doi/10.1103/PhysRev.124.41>

[11] T. Keen, T. Maier, S. Johnston, and P. Lougovski, “Quantum-classical simulation of two-site dynamical mean-field theory on noisy quantum hardware,” *Quantum Science and Technology*, vol. 5, no. 3, p. 035001, apr 2020. [Online]. Available: <https://dx.doi.org/10.1088/2058-9565/ab7d4c>

[12] H. Ma, M. Govoni, and G. Galli, “Quantum simulations of materials on near-term quantum computers,” *npj Computational Materials*, vol. 6, 07 2020. [Online]. Available: <https://www.nature.com/articles/s41524-020-00353-z#Abs1>

[13] E. Gull, A. J. Millis, A. I. Lichtenstein, A. N. Rubtsov, M. Troyer, and P. Werner, “Continuous-time monte carlo methods for quantum impurity models,” *Rev. Mod. Phys.*, vol. 83, pp. 349–404, May 2011. [Online]. Available: <https://link.aps.org/doi/10.1103/RevModPhys.83.349>

[14] U. Schollwöck, “The density-matrix renormalization group in the age of matrix product states,” *Annals of Physics*, vol. 326, no. 1, pp. 96–192, Jan 2011. [Online]. Available: <https://www.sciencedirect.com/science/article/pii/S0003491610001752>

[15] R. Bulla, T. A. Costi, and T. Pruschke, “Numerical renormalization group method for quantum impurity systems,” *Rev. Mod. Phys.*, vol. 80, pp. 395–450, Apr 2008. [Online]. Available: <https://link.aps.org/doi/10.1103/RevModPhys.80.395>

[16] S. McArdle, S. Endo, A. Aspuru-Guzik, S. C. Benjamin, and X. Yuan, “Quantum computational chemistry,” *Rev. Mod. Phys.*, vol. 92, p. 015003, Mar 2020. [Online]. Available: <https://link.aps.org/doi/10.1103/RevModPhys.92.015003>

[17] B. Bauer, D. Wecker, A. J. Millis, M. B. Hastings, and M. Troyer, “Hybrid quantum-classical approach

to correlated materials,” *Phys. Rev. X*, vol. 6, p. 031045, Sep 2016. [Online]. Available: <https://link.aps.org/doi/10.1103/PhysRevX.6.031045>

[18] G. Greene-Diniz, D. Z. Manrique, K. Yamamoto, E. Plekhanov, N. Fitzpatrick, M. Krompiec, R. Sakuma, and D. M. Ramo, “Quantum Computed Green’s Functions using a Cumulant Expansion of the Lanczos Method,” *Quantum*, vol. 8, p. 1383, Jun. 2024. [Online]. Available: <https://doi.org/10.22331/q-2024-06-20-1383>

[19] F. Jamet, A. Agarwal, C. Lupo, D. E. Browne, C. Weber, and I. Rungger, “Krylov variational quantum algorithm for first principles materials simulations,” 2021. [Online]. Available: <https://arxiv.org/abs/2105.13298>

[20] A. Peruzzo, J. McClean, P. Shadbolt, M.-H. Yung, X.-Q. Zhou, P. J. Love, A. Aspuru-Guzik, and J. L. O’Brien, “A variational eigenvalue solver on a photonic quantum processor,” *Nature Commun.*, vol. 5, no. 1, p. 4213, 2014. [Online]. Available: <https://www.nature.com/articles/ncomms5213>

[21] J. R. McClean, J. Romero, R. Babbush, and A. Aspuru-Guzik, “The theory of variational hybrid quantum-classical algorithms,” *New Journal of Physics*, vol. 18, no. 2, p. 023023, feb 2016. [Online]. Available: <https://doi.org/10.1088/1367-2630/18/2/023023>

[22] R. Sakurai, W. Mizukami, and H. Shinaoka, “Hybrid quantum-classical algorithm for computing imaginary-time correlation functions,” *Phys. Rev. Res.*, vol. 4, p. 023219, Jun 2022. [Online]. Available: <https://link.aps.org/doi/10.1103/PhysRevResearch.4.023219>

[23] R. Sakurai, O. J. Backhouse, G. H. Booth, W. Mizukami, and H. Shinaoka, “Comparative study on compact quantum circuits of hybrid quantum-classical algorithms for quantum impurity models,” *Phys. Rev. Res.*, vol. 6, p. 023110, May 2024. [Online]. Available: <https://link.aps.org/doi/10.1103/PhysRevResearch.6.023110>

[24] P. Jordan and E. Wigner, “Über das paulische Äquivalenzverbot,” *Zeitschrift für Physik*, vol. 47, pp. 631–651, 1928.

[25] S. B. Bravyi and A. Y. Kitaev, “Fermionic quantum computation,” *Annals of Physics*, vol. 298, no. 1, pp. 210–226, 2002.

[26] O. Crawford, B. v. Straaten, D. Wang, T. Parks, E. Campbell, and S. Brierley, “Efficient quantum measurement of Pauli operators in the presence of finite sampling error,” *Quantum*, vol. 5, p. 385, Jan. 2021. [Online]. Available: <https://doi.org/10.22331/q-2021-01-20-385>

[27] H.-Y. Huang, R. Kueng, and J. Preskill, “Efficient estimation of pauli observables by derandomization,” *Phys. Rev. Lett.*, vol. 127, p. 030503, Jul 2021. [Online]. Available: <https://link.aps.org/doi/10.1103/PhysRevLett.127.030503>

[28] B. T. Gard, L. Zhu, G. S. Barron, N. J. Mayhall, S. E. Economou, and E. Barnes, “Efficient symmetry-preserving state preparation circuits for the variational quantum eigensolver algorithm,” *npj Quantum Information*, vol. 6, no. 1, Jan. 2020. [Online]. Available: <http://dx.doi.org/10.1038/s41534-019-0240-1>

[29] M. J. D. Powell, *A Direct Search Optimization Method That Models the Objective and Constraint Functions by Linear Interpolation*. Dordrecht: Springer Netherlands, 1994, pp. 51–67. [Online]. Available: [https://doi.org/10.1007/978-94-015-8330-5\\_4](https://doi.org/10.1007/978-94-015-8330-5_4)

[30] D. P. Kingma and J. Ba, “Adam: A method for stochastic optimization,” 2017. [Online]. Available: <https://arxiv.org/abs/1412.6980>

[31] R. H. Byrd, P. Lu, J. Nocedal, and C. Zhu, “A limited memory algorithm for bound constrained optimization,” *SIAM Journal on Scientific Computing*, vol. 16, no. 5, pp. 1190–1208, 1995.

[32] H. J. Vallury, M. A. Jones, C. D. Hill, and L. , “Quantum computed moments correction to variational estimates,” *Quantum*, vol. 4, pp. 373–373, 12 2020. [Online]. Available: <https://quantum-journal.org/papers/q-2020-12-15-373/>

[33] C. Lanczos, “An iteration method for the solution of the eigenvalue problem of linear differential and integral operators,” *Journal of Research of the National Bureau of Standards*, vol. 45, p. 255, 10 1950.

[34] L. C. L. Hollenberg, “Plaquette expansion in lattice hamiltonian models,” *Phys. Rev. D*, vol. 47, pp. 1640–1644, Feb 1993. [Online]. Available: <https://link.aps.org/doi/10.1103/PhysRevD.47.1640>

[35] L. C. L. Hollenberg and N. S. Witte, “Analytic solution for the ground-state energy of the extensive many-body problem,” *Phys. Rev. B*, vol. 54, pp. 16 309–16 312, Dec 1996. [Online]. Available: <https://link.aps.org/doi/10.1103/PhysRevB.54.16309>

[36] L. C. L. Hollenberg and N. S. Witte, “General nonperturbative estimate of the energy density of lattice hamiltonians,” *Phys. Rev. D*, vol. 50, pp. 3382–3386, Sep 1994. [Online]. Available: <https://link.aps.org/doi/10.1103/PhysRevD.50.3382>

[37] R. Haydock, V. Heine, and M. J. Kelly, “Electronic structure based on the local atomic environment for tight-binding bands,” *J. Phys. C: Solid State Phys.*, vol. 5, no. 20, p. 2845, oct 1972. [Online]. Available: <https://doi.org/10.1088/0022-3719/5/20/004>

[38] R. Haydock, “The recursive solution of the schrodinger equation,” ser. Solid State Physics, H. Ehrenreich, F. Seitz, and D. Turnbull, Eds. Academic Press, 1980, vol. 35, pp. 215–294. [Online]. Available: <https://www.sciencedirect.com/science/article/pii/S0081194708605056>